ACS APPLIED ELECTRONIC MATERIALS

Article

Cite This: ACS Appl. Electron. Mater. 2019, 1, 44−50

pubs.acs.org/acsaelm

MBE Growth and Optical Properties of Isotopically Purified ZnSe Heterostructures

Alexander Pawlis,*[,†] Gregor Mussler,[†] Christoph Krause,[†] Benjamin Bennemann,[†] Uwe Breuer,[‡] and Detlev Grützmacher[†]

[†]Peter Grünberg Institut PGI-9, Forschungszentrum Jülich & JARA Jülich-Aachen Research Alliance, D-52425 Jülich, Germany

[‡]Zentralinstitut für Analytik ZEA-3, Forschungszentrum Jülich, D-52425 Jülich, Germany

ABSTRACT: Wide-gap II/VI heterostructures (HS) and quantum wells (QW) composed of ZnSe, CdSe, MgSe, and their ternary and quaternary compounds are attractive candidates for modern quantum optical devices such as single photon sources and optically controlled spin qubits in the visible spectral range. In contrast to similar III/V semiconductor based devices, generally, most of the II/VI compounds allow for isotope purification toward zero-nuclear-spin species in the semiconductor environment. Using the same molecular beam epitaxy (MBE) system for natural and isotopically purified materials opposes the challenge of achieving superior isotope purity, for example, of Zn and Se species on the background of operation of the other effusion cells filled with natural isotopes. Here we report on the crystallographic and optical properties of ZnMgSe/ZnSe heterostructures and quantum wells grown by using ^{64}Zn and ^{80}Se isotopes and Mg with natural isotope distribution. We present a detailed quantitative secondary ion mass spectrometry (SIMS) analysis, which confirms that an extremely high grade of isotope purification of the ZnSe can be maintained, although natural and enriched Zn and Se elements are used in the same MBE system. This pioneering growth study forms a solid base to generate a spin vacuum ZnSe host crystal that is particularly suited for future studies on the dynamics of localized spins in II/VI heterostructures on a strongly extended coherence time scale.

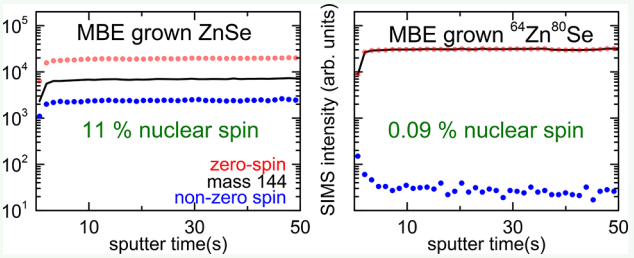

KEYWORDS: *crystal structure, molecular beam epitaxy, heterostructures, optical properties, elementary analysis, isotope purification, X-ray diffraction*

INTRODUCTION

Wide-gap II/VI heterostructures and quantum wells including their ternary and quaternary compounds have been extensively investigated toward their use in optoelectronic devices covering the whole visible spectral range.[1,2] II/VI light-emitting diodes[3,4] and lasers[5−7] were demonstrated and set a high standard on the crystallographic and interface properties of those structures grown on GaAs substrates. However, it turned out that high injection currents or pump powers applied to II/VI based LEDs and lasing devices conducted strong and fast degeneration of the internal quantum efficiency.[4,8] Despite these limitations, MBE grown heterostructures of ZnSe and related materials still feature extremely low defect densities and excellent interface boundaries together with high oscillator strength and utilization to form versatile nanostructures. The latter make wide-gap II/VI semiconductors feasible for low operating power, optically pumped device applications such as low-threshold microdisk lasers in the visible range.[9−12] More recently, inter-sub-band absorption devices in the infrared range[13,14] as well as single photon sources in the visible range[15−17] were demonstrated. Besides such devices, the excellent epilayer properties of ZnSe[18−20] particularly feature basic research studies such as exciton−polariton coupling[21−24] or electron-[25,26] and nuclear-spin dynamics[27] in ZnSe and related materials grown on GaAs substrates.

Paving the way to realize modern qubit devices in most of the common investigated semiconductor systems (e.g., group IV, group III/V, and group II/VI compounds), the interaction between the qubit and the nuclear-spin background of the surrounding semiconductor becomes especially important: Indeed, a limitation of the spin coherence time has been verified for III/V semiconductors,[28,29] in which the non-zero-nuclear-spin background of the material is unavoidable. In contrast, group IV and group II/VI compound semiconductors can be isotopically enriched toward a nuclear-spin depleted host crystal environment.[30] The implementation of phosphorous donor spin qubits embedded in an ^{28}Si isotopically purified host crystal has led to enhancements of the electron-spin coherence by several orders of magnitude.[31] A similar effect has also been observed for donors in isotopically enriched Ge, where the spin coherence strongly depends on the remaining amount of ^{73}Ge in the host crystal.[32] However, as Si and Ge have an indirect bandgap, they are unsuitable for

Received: October 12, 2018
Accepted: December 7, 2018
Published: December 7, 2018

DOI: 10.1021/acsaelm.8b00006
ACS Appl. Electron. Mater. 2019, 1, 44−50

optically controlled spin qubits or efficient single photon sources.

Here, a recently developed suitable alternative is founded on electrons bound to spatially isolated fluorine donors[33,34] in delta-doped or implanted ZnMgSe/ZnSe (e.g., ZnSe:F) QWs. For such material configurations, indistinguishable single photon emitters,[35] postselective polarization entanglement between two sources,[36] and optically addressable spin qubits[37] have already been demonstrated. Exchanging the ZnSe QW epilayer by ZnSe composed of the nuclear-spin zero ^{64}Zn and ^{80}Se isotopes (while the ZnMgSe still can contain its low-cost natural isotope distribution) enforces remarkable potential toward robust stationary quantum memories in ZnSe with much higher coherence times similar as it has been shown for isotopically enriched Si and Ge.

The realization of the MBE growth of ^{64}Zn^{80}Se embedded in an HS containing epilayers of other II/VI elements with natural isotope distribution poses significant challenges. Using the same MBE system for natural and isotopically purified II/VI species provides the flexibility for the growth of high-quality heterostructures composed of combinations of natural, nuclear-spin diluted, and nuclear-spin-free II/VI epilayers. However, cross-contamination of the evaporation cells containing the extremely expensive isotopically purified materials with the natural isotopes used in the same MBE chamber must be minimized. To meet these requirements, we used specifically constructed effusion cells provided by *Createc*[38] (described in Experimental Details).

In this paper, we present a quantitative SIMS analysis, which confirms isotope purities in the ^{64}Zn^{80}Se epilayers close to those of the original grade of source elements (e.g., depending only on the commercial available element purity), despite the fact that natural and enriched elementary source materials are used in the same MBE system. Moreover, we report on the crystallographic and optical properties of ZnMgSe/ZnSe HSs and QWs as-grown using ^{64}Zn and ^{80}Se isotopes and Mg with natural isotope distribution. This pioneering growth study forms a solid base to generate a spin-vacuum ZnSe host crystal that is particularly suited for future studies on the dynamics of an ensemble or single localized spins in isotopically enriched II/VI heterostructures featuring a strongly extended coherence time scale.

EXPERIMENTAL DETAILS

The ZnMgSe/ZnSe heterostructures and QWs were grown on (001)-GaAs substrates. Prior to the II/VI growth, the epiready substrates were transferred into a III/V growth chamber for thermal deoxidation followed by the growth of a ~500 nm thick and undoped GaAs buffer layer. Via in situ ultrahigh vacuum transfer, the samples were subsequently loaded in the II/VI MBE growth chamber. The MBE chamber contains sources for natural isotopes of Zn, Cd, Mg, and Se as well as the specially designed effusion cells for isotopically enriched ^{64}Zn and ^{80}Se. These effusion cells are constructed with advanced shutter elements including a linear shift that allows the cell opening to be sealed at standby temperature from any direct contamination by the other cells in the chamber. Moreover, to minimize consumption of the highly expensive isotopically enriched materials, the heater stage and crucible volume of the cells was tailored to fast temperature adjustment and flux stabilization within about 30 min.

The II/VI growth of the HSs and QWs was performed at a substrate temperature of 290°C and under Se-rich conditions. Firstly, an ~10 nm thick buffer layer of ZnSe was deposited at a slightly lower substrate temperature to maintain a smooth and abrupt III/V−II/VI interface. Subsequently, two types of sample structures were grown: the HSs consist of a 15 nm thick ZnMgSe barrier with about 8% Mg content and a 70 nm thick, fluorine-doped ZnSe layer. The QWs are formed by a 15 nm thick and fluorine-doped ZnSe layer in between two 25 nm thick ZnMgSe barriers with approximately the same composition as the heterostructures. Representative cross section drawings of HS and QW sample structures are illustrated in the insets of Figure 3a,c, and an overview of all samples used for this study is given in Table 1. Due to the overall II/VI sample stack thickness of about 70−90 nm and the low magnesium content, all layers are fully compressively strained on the GaAs substrate (confirmed by asymmetric reciprocal space maps not shown here). The fluorine doping was performed by using a ZnF_2 cracker cell. For both types of sample structures (HS and QW), the fluorine concentration was varied between 10^{15} and 10^{18} cm^{-3} and confirmed by SIMS analysis of the corresponding HS samples. If not further mentioned, the Zn and Se species in each layer of the HS and QW structures contain isotopically purified ^{64}Zn and ^{80}Se elements, while the Mg is composed of its natural isotope distribution. Additionally, an as-grown and fluorine-doped ZnSe reference sample (sample R) containing only the natural isotope distribution of ZnSe was grown to verify our quantitative SIMS isotope analysis discussed below.

Table 1. Overview of the HS and QW Structures Investigated for This Study[a]

sample	nr.	type (HS/QW)	F-content (10^{16}cm^{-3})
A	0093	HS	≤3
B	0100	HS	10
C	0095	HS	200
D	0094	QW	≤3
E	0101	QW	10
F	0102	QW	200

[a]Samples A and D are unintentionally doped. The F-content is upper-bound by the SIMS detection limit of about 3 × 10^{16}cm^{-3}.

The isotopically purified ^{64}Zn and ^{80}Se cell materials were company-specified with a remaining non-zero-spin content of $N(^{67}\mathrm{Zn}) \leq 0.04\%$ and $N(^{77}\mathrm{Se}) \leq 0.01\%$ (atomic percent), which forms the lower-bound limit of any possible purification grade in our MBE chamber. For the SIMS analysis, we have chosen the $(^{X}\mathrm{Zn}^{Y}\mathrm{Se})^{-}$ signal, which provides an excellent dynamic range of intensities for all stable isotope configurations in ZnSe. The latter spans the mass range between 138 and 152 amu for any combination of the following isotopes of Zn and Se with their corresponding occurrences: $N(^{64}\mathrm{Zn}) = 49.17\%$, $N(^{66}\mathrm{Zn}) = 27.73\%$, $N(^{67}\mathrm{Zn}) = 4.04\%$, $N(^{68}\mathrm{Zn}) = 18.45\%$, $N(^{70}\mathrm{Zn}) = 0.61\%$ as well as $N(^{74}\mathrm{Se}) = 0.89\%$, $N(^{76}\mathrm{Se}) = 9.37\%$, $N(^{77}\mathrm{Se}) = 7.63\%$, $N(^{78}\mathrm{Se}) = 23.77\%$, $N(^{80}\mathrm{Se}) = 49.61\%$, $N(^{82}\mathrm{Se}) = 8.73\%$ according to Ref 39 and references therein. The SIMS analyses were done using a dual beam TOF-SIMS IV by ION-TOF GmbH. A Cs^+ beam with an energy of 1 keV was raster scanned over an area of 300 × 300 μm^2 for sputtering. A pulsed Bi^{3+} ion beam of 25 keV was scanned in the center of the sputtered area within 50 μm^2. These ns-pulses generate the secondary ions for the time of flight mass spectrometer analysis. The system is registering the complete mass spectra up to 300 amu.

X-ray measurements were accomplished with a high-resolution Bruker D8 diffractometer. Conventional $2\theta/\omega$-scans around the (004) reflection of the GaAs substrate were carried out with a mechanical slit of 0.1 mm at the detector side. For rocking curves, a double Ge monochromator at the detector side was employed to achieve ultrahigh resolution. The $2\theta/\omega$-scans were accomplished in a range from $2\theta = 62-70°$ with an angular resolution of 0.005°. For the rocking curves, the angular resolution of 0.0002° was chosen.

The photoluminescence (PL) studies were carried out in a μ-PL setup with a cold-finger cryostat operated at about 10 K. For excitation, a pulsed laser source (10 MHz repetition rate, ~1 ps pulse length) emitting at 397 nm wavelength was used and focused down to a spot size of about 2 μm diameter.

DOI: 10.1021/acsaelm.8b00006
ACS Appl. Electron. Mater. 2019, 1, 44−50

RESULTS AND DISCUSSIONS

Because of the joint use of naturally distributed and isotopically enhanced cell materials for Zn and Se, cross-contamination might lead to a substantially reduced grade of purification of the as-grown heterostructures. As mentioned above, we investigated this issue by a detailed quantitative SIMS intensity analysis of the isotopically purified samples A, B, and C and compared the results with the reference sample R, which contains the natural isotope distribution of Zn and Se. Figure 1a shows the background-corrected SIMS intensity

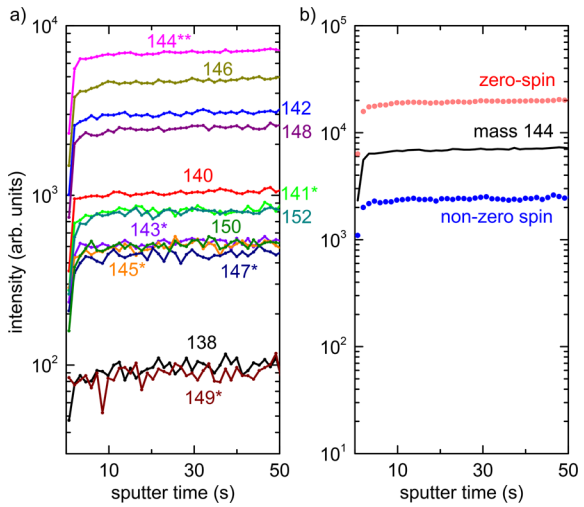

Figure 1. SIMS profiles of sample R containing the natural distribution of Zn and Se isotopes. (a) Intensity tracks of $(^{X}Zn^{Y}Se)^{-}$ combinations for each relevant atomic mass. Stars indicate masses containing the non-zero isotopes. (b) Compressed view of the SIMS data with summed up intensities of all zero- and non-zero-spin isotopes (red and blue) as well as the reference mass 144 amu mainly contributed by $(^{64}Zn^{80}Se)^{-}$.

signal tracks of $(^{X}Zn^{Y}Se)^{-}$ obtained from the reference sample R. Its natural isotope distribution is reflected in different absolute intensities of the mass signals. Apart from the intensities at 138 and 152 amu corresponding solely to $(^{64}Zn^{74}Se)^{-}$ and $(^{70}Zn^{82}Se)^{-}$, all other mass tracks contain intensities from several different $(^{X}Zn^{Y}Se)^{-}$ species leading to the same atomic mass. Generally, all odd masses contain intensity contributions of either ^{67}Zn or ^{77}Se with non-zero nuclear spin, while zero nuclear spin of Zn and Se is provided in the case of all even masses except 144 amu. The latter mass signal includes a small intensity fraction (~0.3%) related to the $(^{67}Zn^{77}Se)^{-}$ species with non-zero nuclear spin of both elements. The more convenient, compressed visualization of the same SIMS measurement is presented in Figure 1b by summation of the intensity tracks of all zero (red dots) and non-zero-nuclear-spin species (blue dots). For reference, the total intensity obtained at 144 amu (black line) is also included in Figure 1b.

Our quantitative analysis of the SIMS data and subsequent extraction of the non-zero-nuclear-spin content in all HS samples is based on the following suppositions: Firstly, we assume that ionization probability and detection efficiency of all $(^{X}Zn^{Y}Se)^{-}$ is the same. Consequently, SIMS intensities obtained for each mass track are proportional to the product of the occurrences of any Zn and Se isotope combination that contributes to the corresponding mass track. Secondly, for the analysis of the isotopically purified samples A, B, and C only, we neglect the contribution of the isotope $(^{67}Zn^{77}Se)^{-}$ to the SIMS intensity at 144 amu. This constraint is applicable but leads to an absolute error of about 0.003% in the remaining amount of non-zero-spin isotopes for calculation of the isotope purification grade (IPG). The latter is defined by the ratio of the normalized total amount of non-zero-nuclear-spin intensity of sample R divided by that of each of the purified samples A, B, and C, respectively.

From the SIMS data of sample R in Figure 1, we extracted the quantitative natural isotope distribution in $(^{X}Zn^{Y}Se)^{-}$ to verify our previously discussed model approach. The results are depicted in Table 2 as a function of the isotope mass of ZnSe.

Table 2. Calculation Results $I(m)$, $I(^{77}Se,m)$, $I(^{67}Zn,m)$ of the Natural Non-Zero Isotope Distribution of ZnSe in the Reference Sample R and Literature Values $P(m)$ of the Corresponding Non-Zero Isotope Fraction at Mass m Derived from Ref 39[a]

mass m (amu)	$I_{int,m}$	$I(m)$ (%)	$P(m)$ (%)	$I(^{77}Se,m)$ (%)	$I(^{67}Zn,m)$ (%)
138	2442.1	0.446	0.438	0	0
140	25 848.9	4.717	4.854	0	0
141	20 353.5	3.714	3.788	3.679	0.035
142	75 677.6	13.811	14.450	0	0
143	13 125.7	2.395	2.494	2.032	0.364
144	173 078.8	31.585	33.027	0.295	0.295
145	12 461.8	2.274	2.368	1.352	0.922
146	117 080.4	21.366	22.492	0	0
147	11 114.4	2.028	2.051	0.046	1.982
148	61 930.9	11.302	11.719	0	0
149	2203.4	0.402	0.353	0	0.402
150	12 778.4	2.332	1.913	0	0
152*	19 874.1*	3.627*	0.053	0	0
Σ	547 970.1			7.404	4.000

[a]The mass signal at 152 amu (indicated by stars) strongly deviates from the literature value and might be due to an unknown impurity complex.

The parameters in Table 2 are defined as follows: $I_{int,m}$ corresponds to the integrated SIMS intensities of each mass track over 9–40 s sputter time (x axis in Figure 1). This interval was specifically chosen in order to avoid unstable SIMS signal due to surface effects (0–9 s) and change of the crystal matrix when the ion milling penetrates into the ZnMgSe barrier of the heterostructures (≥ 40 s). I_{total} is the overall intensity of all SIMS signals in the same sputter time interval. $I(m) = \frac{I_{int,m}}{I_{total}}$ is the fraction of SIMS intensity at mass m. The value $P(m)$ is obtained by considering the literature values[39] of occurrence of all $(^{X}Zn^{Y}Se)^{-}$ isotope configurations contributing to the specific mass m. Finally, $I(^{77}Se,m)$ and $I(^{67}Zn,m)$ represent the fraction of the measured SIMS intensity $I(m)$ distributed between the non-zero-nuclear-spin isotopes ^{77}Se and ^{67}Zn, respectively. In the case of all atomic masses except 152 amu, the measured SIMS intensity $I(m)$ is in excellent agreement with the occurrences $P(m)$ of the non-zero isotopes. The deviation at 152 amu might be explained by the detection of an additional impurity complex such as CsF, as the sputter source is Cs, and all samples are fluorine-doped. However, this deviation is irrelevant for the analysis of the isotopically purified samples, as mass 152 amu does not

DOI: 10.1021/acsaelm.8b00006
ACS Appl. Electron. Mater. 2019, 1, 44–50

contain any Zn and Se species with non-zero nuclear spin. By summation over all contributing masses, we obtained the individual non-zero-spin content of both species $N(^{77}Se)$ = 7.404% and $N(^{67}Zn)$ = 4.000% in sample R. Excluding the SIMS intensity track at mass 152 amu from our analysis (e.g., overall intensity contribution of 0.053%) the results yield $N(^{77}Se)$ = 7.68 ± 0.05% and $N(^{67}Zn)$ = 4.15 ± 0.05%. Both are in good agreement with the corresponding literature values of $N(^{77}Se)$ = 7.63% and $N(^{67}Zn)$ = 4.04%, which confirms the validity of our quantitative SIMS analysis.

The diagrams in Figure 2 show the SIMS intensity profiles (in compressed form) of all HS samples we investigated in this

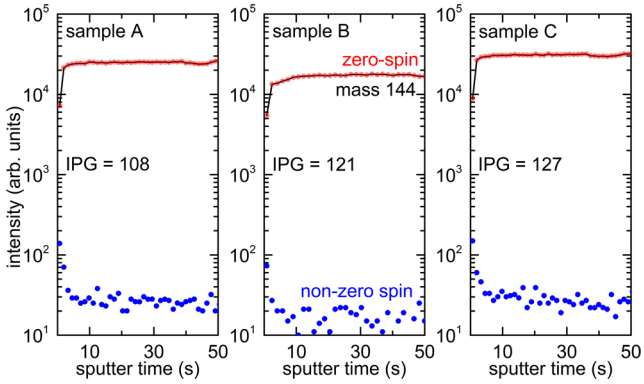

Figure 2. Compressed forms of the SIMS profiles of as-grown isotopically purified HS samples A, B, and C. Intensity contributions of zero-spin (red), non-zero-spin (blue), and the reference 144 amu (black) isotopes are shown. The IPGs of all samples are higher than 100, which confirms strong suppression of the non-zero-spin components ^{67}Zn and ^{77}Se.

study. The reference signal at 144 amu (black curve) mainly stems from the $(^{64}Zn^{80}Se)^-$ isotope and provides nearly the same intensity as the sum of all zero-spin configurations (red dots). The intensity track of the sum of all remaining non-zero-spin species is about 3 orders of magnitude lower, which compared to the natural isotope distribution of sample R (see Figure 1b) roughly containing 11 % of non-zero-spin, leads to an overall purification grade on the order of 100. Using our previously described model approach, we derive individual IPGs of 108, 121, and 127 for the samples A, B, and C, respectively. For the HS with the highest IPG (sample C), the remaining non-zero-spin contents reveal $N(^{77}Se)$ = 0.050 ± 0.003% and $N(^{67}Zn)$ = 0.040 ± 0.003%. Note that these values are close to the limits in the available purification grades of the cell materials (e.g., $N(^{77}Se) \leq 0.01\%$ and $N(^{67}Zn) \leq 0.04\%$). Concluding the above described SIMS analysis, only marginal cross-contamination appears between naturally distributed and isotopically enriched Zn and Se species evaporated from effusion cells operated in the same MBE chamber.

Besides the comprehensive SIMS analysis, we performed a general structural characterization of the HSs and QWs with high-resolution x-ray diffraction (XRD). Figure 3 shows the XRD measurements of two selected ones, the heterostructure sample B and the quantum well sample E. Figure 3a presents a $2\theta/\omega$-scan across the (004) reflexes of the GaAs substrate and the epilayers of sample B (dots). Pronounced thickness oscillations confirm abrupt, planar interface morphologies between the different epilayers of the HS. The peak of the ZnSe-(004) reflex is found at an angular position around 2Θ = 65.6°, which indicates that the ZnSe:F layer is pseudomorph-

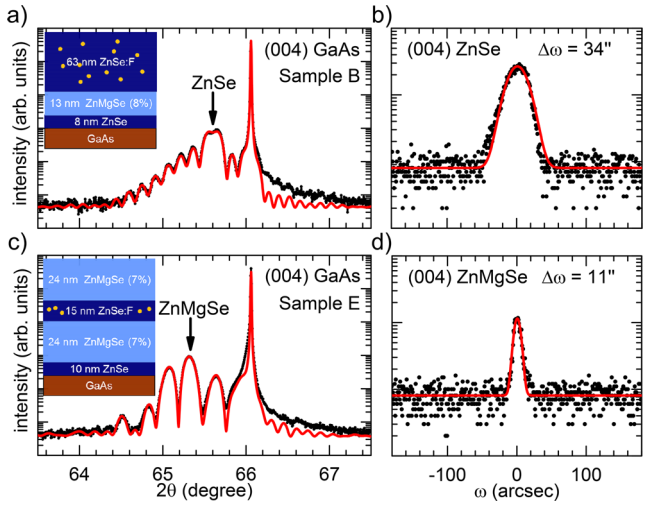

Figure 3. XRD analysis of representative samples B and E. (a) High-resolution $2\theta/\omega$-scan across the 004 reflexes of the HS sample B (dots) and corresponding best-fit calculation of the data (red line). From the latter, the real sample structure shown in the inset is derived. (b) ω-Scan across the 004 reflex of ZnSe (dots) and Gaussian fit (red line) to quantify the line width of the reflex. (c) Same as in (a) but obtained for the QW sample E with corresponding sample structure shown in the inset. (d) ω-Scan of the 004 reflex of the ZnMgSe barriers (dots) and corresponding Gaussian fit (red line).

ically strained on the GaAs substrate. The strain status was also confirmed by a reciprocal space map (RSM) measured around the (224) reflex (not shown here). The asymmetric shape at the lower angle tail of the ZnSe-(004) reflex might be attributed to intensity from the ZnMgSe barrier underneath the ZnSe:F layer. The schematic drawing (inset of Figure 3a) is the sample structure we derived from a best-fit simulation (red line) of the experimental data using full-dynamic X-ray scattering theory. The magnesium concentration of about 8% and the width of the epilayers is in good agreement with the presumed MBE growth parameters. Figure 3b represents the rocking curve (ω-scan) of the (004)-ZnSe reflex (dots). Besides the coherent scattering peak with a full width at half maximum (FWHM) line width of about 34″, no diffusive background contribution is resolved. Although the obtained FWHM is about 3 times higher than the resolution limit of the diffractometer, it still confirms a low defect density in the ZnSe:F epilayer.

The $2\theta/\omega$-scan and rocking curve of the QW sample E are presented in Figure 3c,d. Again, the schematic drawing in the inset shows the sample structure obtained from the best-fit simulation of the experimental data in Figure 3c. Due to the magnesium concentration of about 7%, the (004)-ZnMgSe reflex of the barrier layers is located at an angular position of 2Θ = 65.3°. The excellent structural quality and extremely low defect density of sample E are reflected by the FWHM of the rocking curve of the ZnMgSe-(004) reflex shown in Figure 3d. Here we measured a line width of about 11″, which is close to the resolution limit of the diffractometer. Note that similar to that in Figure 3b, the rocking curve only contains the coherent scattering peak and does not denote any diffusive scattering that is frequently observed in HSs and QWs with moderate or high interface defect densities.[40] Remarkably, the FWHM of the rocking curve of the QW sample E in Figure 3d is substantially smaller than that of the HS sample B (Figure 3b). The increased line width of the HS might stem from the onset

DOI: 10.1021/acsaelm.8b00006
ACS Appl. Electron. Mater. 2019, 1, 44−50

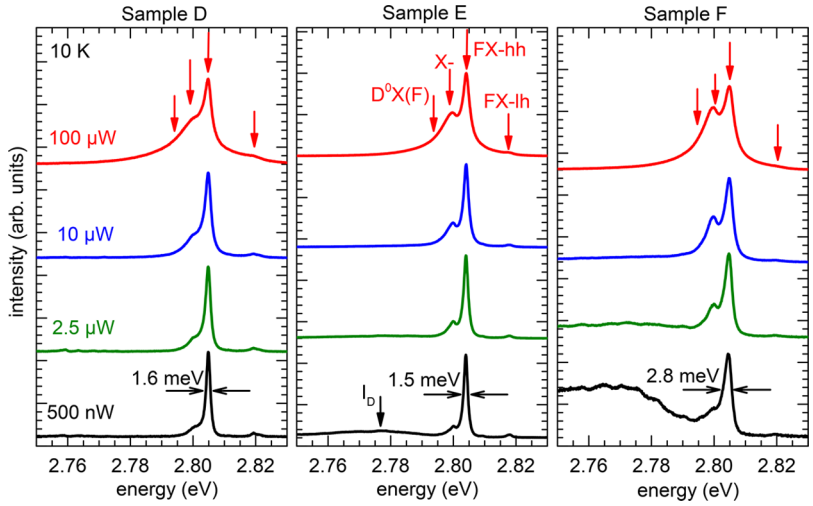

Figure 4. Low-temperature (10 K) and power-dependent PL spectra of the QW samples E, F, and G. The fluorine doping concentration increases from E to G between 10^{16}–10^{18} cm^{-3}. The relevant excitonic transitions expected for strained ZnSe QWs on GaAs, namely heavy- and light-hole free-exciton transitions (FX-hh, FX-lh) as well as charged exciton transition (X^-) and fluorine donor-bound exciton transition ($D^0X(F)$) with heavy-hole contribution, are indicated by the arrows.

of relaxation of the ZnSe:F epilayer (which was not resolved in the RSM) and/or related to the homogeneous fluorine doping, while the barriers of the QW samples were left undoped.

We performed a power-dependent photoluminescence study of all QWs at low temperatures (about 10 K) to investigate the optical properties of the isotopically purified samples. The spectra are shown in Figure 4 for excitation powers between 500 nW and 100 μW. For all three QWs, the relevant excitonic transitions (indicated by the arrows) in compressively strained ZnSe QWs on GaAs are clearly determined. The fluorine doping concentration was changed by about 2 orders of magnitude (e.g., $\leq 3 \times 10^{16}$ to 2×10^{18} cm^{-3}) from samples E to G. Note that the FWHM line width of the dominant free-exciton transition (FX-hh at 2.804 eV) is only about 1.6 meV at low excitation powers, which confirms very low interface discontinuity/roughness of the QWs as also inferred from the HRXRD measurements (Figure 3). The two further transitions labeled X^- and $D^0X(F)$ are pronounced visible at higher excitation powers. Both are related to fluorine donors and can be identified as the neutral donor-bound exciton transition at 2.794 eV and a charged exciton (trion) at 2.797 eV. The latter stems from a significant free carrier concentration in the ZnSe QW. The intensity of both peaks substantially increases from samples E to G, i.e., with rising fluorine content.

Line width and energetic position of the transitions in the PL spectra in Figure 4 coincide with those frequently measured in fluorine-doped ZnSe QWs grown with a natural isotope distribution of Zn and Se (see, for examples, Refs 11, 18, 25, and 41). At considerably high fluorine doping concentrations (samples E and F), a broad deep impurity emission (I_D) around 2.777 eV is observed and can be attributed to acceptor complexes or Zn vacancies in the QW. Those might be induced by ZnF_2 molecules or when fluorine atoms are incorporated interstitial lattice sites. However, the deep level band emission saturates in intensity already at excitation powers of 2.5–10 μW, which indicates a considerably low density of such point defects.

Finally, we would like to highlight the enormous potential of our as-grown $^{64}Zn^{80}Se$ QWs for application as spin-selective single photon sources or optically controllable spin qubits: Considering a typical Bohr radius of 2–3 nm for fluorine donor-bound excitons in ZnSe together with the above achieved isotope purification grade, one can extract the remaining nuclear-spin quantity within the bound exciton volume. Using the best achieved IPG of 127 from this study, in average, about 0.4–1.2 ^{77}Se and 0.3–1.0 ^{67}Zn nuclear spins, respectively, remain per exciton volume. Consequently, the current purification grade is already sufficient to study single fluorine qubits in a zero nuclear-spin ZnSe environment with substantial probability.

SUMMARY

In conclusion, we have investigated isotopically purified and fluorine-doped ZnMgSe/ZnSe heterostructures and quantum wells that were grown in an MBE chamber containing effusion cells of natural and purified Zn and Se isotopes at the same time. Quantitative SIMS measurements of the isotope distribution in the as-grown samples confirmed extremely high purification grades IPG $\geq$ 100 in the nuclear-spin-free epilayers compared to those with natural isotope composition. This confirms that cross-contamination between the different Zn and Se species in the same MBE chamber is negligible. Regarding the structural properties of HSs and QWs grown with $^{64}Zn^{80}Se$ epilayers, HRXRD investigations confirmed abrupt interfaces and low defect densities as that of the GaAs substrates. Optical properties of fluorine-doped $^{64}Zn^{80}Se$ QWs revealed similar characteristics as fluorine-doped ZnSe QWs containing the natural isotope distribution. Altogether, our pioneering growth study demonstrates the generation of a nuclear-spin-free ZnSe host crystal, which opens up enormous potential for future studies on the dynamics of localized electron spins in ZnSe on a strongly extended coherence scale.

AUTHOR INFORMATION

Corresponding Author

*E-mail: a.pawlis@fz-juelich.de.

ORCID

Alexander Pawlis: 0000-0002-3394-0707

Notes

The authors declare no competing financial interest.

DOI: 10.1021/acsaelm.8b00006
ACS Appl. Electron. Mater. 2019, 1, 44–50

■ ACKNOWLEDGMENTS

We acknowledge the financial support by the Deutsche Forschungsgemeinschaft in the frame of the ICRC TRR-160 and Grant No. PA 1976/4-1 as well as the Volkswagen Foundation (Project No. 88360/90080). We thank Createc Fischer & Co. GmbH for their fruitful technical support and design of the effusion cells for the isotopically purified elements.

■ REFERENCES

(1) Eason, D.; Yu, Z.; Hughes, W.; Roland, W.; Boney, C.; Cook, J.; Schetzina, J.; Cantwell, G.; Harsch, W. High-Brightness Blue and Green Light-Emitting-Diodes. *Appl. Phys. Lett.* **1995**, *66*, 115−117.

(2) Perez-Paz, M.; Zhou, X.; Munoz, M.; Sohel, M.; Lu, H.; Fernandez, F.; Jean-Mary, F.; Akins, D.; Tamargo, M. Single Layer and Stacked CdSe Self-Assembled Quantum Dots with ZnCdMgSe Barriers for Visible and White Light Emitters. *J. Vac. Sci. Technol., B: Microelectron. Process. Phenom.* **2005**, *23*, 1236−1239.

(3) Nishizawa, J. I.; Itoh, K.; Okuno, Y.; Sakurai, F. Blue Light Emission from ZnSe p-n Junctions. *J. Appl. Phys.* **1985**, *57*, 2210−2216.

(4) Gordeev, N.; Ivanov, S.; Kopchatov, V.; Novikov, I.; Shubina, T.; Il'inskaya, N.; Kop'ev, P.; Reuscher, G.; Waag, A.; Landwehr, G. Improved Degradation Stability of Blue-Green II-VI Light-Emitting Diodes with Excluded Nitrogen-Doped ZnSe-Based Layers. *Semiconductors* **2001**, *35*, 1340−1344.

(5) Nakanishi, F.; Doi, H.; Okuda, N.; Matsuoka, T.; Katayama, K.; Saegusa, A.; Matsubara, H.; Yamada, T.; Uemura, T.; Irikura, M.; Nishine, S. Low-Threshold Room-Temperature CW Operation of ZnSe-Based Blue/Green Laser Diodes Grown on Conductive ZnSe Substrates. *Electron. Lett.* **1998**, *34*, 496−497.

(6) Kruse, C.; Lohmeyer, H.; Sebald, K.; Gutowski, J.; Hommel, D.; Wiersig, J.; Jahnke, F. Green Laser Emission from Monolithic II-VI-Based Pillar Microcavities near Room Temperature. *Appl. Phys. Lett.* **2008**, *92*, 031101.

(7) Klein, T.; Klembt, S.; Kozlovsky, V. I.; Zheng, A.; Tiberi, M. D.; Kruse, C. High-Power Green and Blue Electron-Beam Pumped Surface-Emitting Lasers Using Dielectric and Epitaxial Distributed Bragg Reflectors. *J. Appl. Phys.* **2015**, *117*, 113106.

(8) Hovinen, M.; Ding, J.; Salokatve, A.; Nurmikko, A. V.; Hua, G. C.; Grillo, D. C.; He, L.; Han, J.; Ringle, M.; Gunshor, R. L. On Degradation of ZnSe-Based Blue-Green Diode Lasers. *J. Appl. Phys.* **1995**, *77*, 4150−4152.

(9) Hovinen, M.; Ding, J.; Nurmikko, A. V.; Grillo, D. C.; Han, J.; He, L.; Gunshor, R. L. Blue-Green Laser Emission from ZnSe Quantum Well Microresonators. *Appl. Phys. Lett.* **1993**, *63*, 3128−3130.

(10) Renner, J.; Worschech, L.; Forchel, A.; Mahapatra, S.; Brunner, K. CdSe Quantum Dot Microdisk Laser. *Appl. Phys. Lett.* **2006**, *89*, 231104.

(11) Pawlis, A.; Panfilova, M.; Sanaka, K.; Ladd, T. D.; As, D. J.; Lischka, K.; Yamamoto, Y. Low-Threshold ZnSe Microdisk Laser Based on Fluorine Impurity Bound-Exciton Transitions. *Microelectron. J.* **2009**, *40*, 256−258.

(12) Ruth, M.; Finke, A.; Schmidt, G.; Reuter, D.; Scholz, S.; Ludwig, A.; Wieck, A. D.; Pawlis, A. Optical Properties of Strain-Compensated CdSe/ZnSe/(Zn,Mg)Se Quantum Well Microdisks. *Opt. Express* **2015**, *23*, 29079−29088.

(13) De Jesus, J.; Chen, G.; Hernandez-Mainet, L. C.; Shen, A.; Tamargo, M. C. Strain Compensated CdSe/ZnSe/ZnCdMgSe Quantum Wells as Building Blocks for Near to Mid-IR Intersubband Devices. *J. Cryst. Growth* **2015**, *425*, 207−211.

(14) Chen, G.; Tamargo, M. C.; Shen, A. MgSe/CdSe Coupled Quantum Wells with Optimized MgSe Coupling Layer Thickness and Near Infrared Intersubband Absorption around 1.55 μ m. *J. Phys. D: Appl. Phys.* **2016**, *49*, 115111.

(15) Sebald, K.; Michler, P.; Passow, T.; Hommel, D.; Bacher, G.; Forchel, A. Single-Photon Emission of CdSe Quantum Dots at Temperatures up to 200 K. *Appl. Phys. Lett.* **2002**, *81*, 2920−2922.

(16) Strauf, S.; Michler, P.; Klude, M.; Hommel, D.; Bacher, G.; Forchel, A. Quantum Optical Studies on Individual Acceptor Bound Excitons in a Semiconductor. *Phys. Rev. Lett.* **2002**, *89*, 177403.

(17) De Greve, K.; Clark, S. M.; Sleiter, D.; Sanaka, K.; Ladd, T. D.; Panfilova, M.; Pawlis, A.; Lischka, K.; Yamamoto, Y. Photon Antibunching and Magnetospectroscopy of a Single Fluorine Donor in ZnSe. *Appl. Phys. Lett.* **2010**, *97*, 241913.

(18) Pawlis, A.; Berstermann, T.; Brüggemann, C.; Bombeck, M.; Dunker, D.; Yakovlev, D. R.; Gippius, N. A.; Lischka, K.; Bayer, M. Exciton States in Shallow ZnSe/(Zn,Mg)Se Quantum Wells: Interaction of Confined and Continuum Electron and Hole States. *Phys. Rev. B: Condens. Matter Mater. Phys.* **2011**, *83*, 115302.

(19) Finke, A.; Ruth, M.; Scholz, S.; Ludwig, A.; Wieck, A. D.; Reuter, D.; Pawlis, A. Extending the Spectral Range of CdSe/ZnSe Quantum Wells by Strain Engineering. *Phys. Rev. B: Condens. Matter Mater. Phys.* **2015**, *91*, 035409.

(20) Rieger, T.; Riedl, T.; Neumann, E.; Gruetzmacher, D.; Lindner, J. K. N.; Pawlis, A. Strain Compensation in Single ZnSe/CdSe Quantum Wells: Analytical Model and Experimental Evidence. *ACS Appl. Mater. Interfaces* **2017**, *9*, 8371−8377.

(21) Pawlis, A.; Khartchenko, A.; Husberg, O.; As, D.; Lischka, K.; Schikora, D. Large Room Temperature Rabi-Splitting in a ZnSe/(Zn,Cd)Se Semiconductor Microcavity Structure. *Solid State Commun.* **2002**, *123*, 235−238.

(22) Markov, S.; Seisyan, R.; Kosobukin, V. Spectroscopy of Excitonic Polaritons in Strained II-VI Semiconductor Structures with Wide Quantum Wells. *Semiconductors* **2004**, *38*, 225−231.

(23) Curran, A.; Morrod, J. K.; Prior, K. A.; Kar, A. K.; Warburton, R. J. Exciton-Photon Coupling in a ZnSe-Based Microcavity Fabricated Using Epitaxial Liftoff. *Semicond. Sci. Technol.* **2007**, *22*, 1189−1192.

(24) Sebald, K.; Seyfried, M.; Klembt, S.; Bley, S.; Rosenauer, A.; Hommel, D.; Kruse, C. Strong Coupling in Monolithic Microcavities with ZnSe Quantum Wells. *Appl. Phys. Lett.* **2012**, *100*, 161104.

(25) Greilich, A.; Pawlis, A.; Liu, F.; Yugov, O. A.; Yakovlev, D. R.; Lischka, K.; Yamamoto, Y.; Bayer, M. Spin Dephasing of Fluorine-Bound Electrons in ZnSe. *Phys. Rev. B: Condens. Matter Mater. Phys.* **2012**, *85*, 121303.

(26) Heisterkamp, F.; Zhukov, E. A.; Greilich, A.; Yakovlev, D. R.; Korenev, V. L.; Pawlis, A.; Bayer, M. Longitudinal and Transverse Spin Dynamics of Donor-Bound Electrons in Fluorine-Doped ZnSe: Spin Inertia Versus Hanle Effect. *Phys. Rev. B: Condens. Matter Mater. Phys.* **2015**, *91*, 235432.

(27) Zhukov, E. A.; Kirstein, E.; Kopteva, N. E.; Heisterkamp, F.; Yugova, I. A.; Korenev, V. L.; Yakovlev, D. R.; Pawlis, A.; Bayer, M.; Greilich, A. Discretization of the Total Magnetic Field by the Nuclear Spin Bath in Fluorine-Doped ZnSe. *Nat. Commun.* **2018**, *9*, 1941.

(28) Khaetskii, A.; Loss, D.; Glazman, L. Electron Spin Decoherence in Quantum Dots due to Interaction with Nuclei. *Phys. Rev. Lett.* **2002**, *88*, 186802.

(29) Clark, S. M.; Fu, K.-M. C.; Zhang, Q.; Ladd, T. D.; Stanley, C.; Yamamoto, Y. Ultrafast Optical Spin Echo for Electron Spins in Semiconductors. *Phys. Rev. Lett.* **2009**, *102*, 247601.

(30) Lauck, R.; Schonherr, E. Isotopically Pure ZnSe Crystals Grown from the Vapor. *J. Cryst. Growth* **1999**, *197*, 513−516.

(31) Tyryshkin, A. M.; Tojo, S.; Morton, J. J. L.; Riemann, H.; Abrosimov, N. V.; Becker, P.; Pohl, H.-J.; Schenkel, T.; Thewalt, M. L. W.; Itoh, K. M.; Lyon, S. A. Electron Spin Coherence Exceeding Seconds in High-Purity Silicon. *Nat. Mater.* **2012**, *11*, 143−147.

(32) Sigillito, A. J.; Jock, R. M.; Tyryshkin, A. M.; Beeman, J. W.; Haller, E. E.; Itoh, K. M.; Lyon, S. A. Electron Spin Coherence of Shallow Donors in Natural and Isotopically Enriched Germanium. *Phys. Rev. Lett.* **2015**, *115*, 247601.

(33) Pawlis, A.; Sanaka, K.; Gotzinger, S.; Yamamoto, Y.; Lischka, K. Investigation of Excitons Bound to Fluorine Donors in ZnSe. *Semicond. Sci. Technol.* **2006**, *21*, 1412−1415.

DOI: 10.1021/acsaelm.8b00006
ACS Appl. Electron. Mater. 2019, 1, 44−50

(34) Kim, Y. M.; Sleiter, D.; Sanaka, K.; Yamamoto, Y.; Meijer, J.; Lischka, K.; Pawlis, A. Semiconductor Qubits Based on Fluorine Implanted ZnMgSe/ZnSe Quantum-Well Nanostructures. *Phys. Rev. B: Condens. Matter Mater. Phys.* **2012**, *85*, 085302.
(35) Sanaka, K.; Pawlis, A.; Ladd, T. D.; Lischka, K.; Yamamoto, Y. Indistinguishable Photons from Independent Semiconductor Nanostructures. *Phys. Rev. Lett.* **2009**, *103*, 053601.
(36) Sanaka, K.; Pawlis, A.; Ladd, T. D.; Sleiter, D. J.; Lischka, K.; Yamamoto, Y. Entangling Single Photons from Independently Tuned Semiconductor Nanoemitters. *Nano Lett.* **2012**, *12*, 4611−4616.
(37) Sleiter, D. J.; Sanaka, K.; Kim, Y. M.; Lischka, K.; Pawlis, A.; Yamamoto, Y. Optical Pumping of a Single Electron Spin Bound to a Fluorine Donor in a ZnSe Nanostructure. *Nano Lett.* **2013**, *13*, 116−120.
(38) CreaTec Fischer & Co. GmbH. https://www.createc.de/Germany/.
(39) Berglund, M.; Wieser, M. E. Isotopic Compositions of the Elements 2009 (IUPAC Technical Report). *Pure Appl. Chem.* **2011**, *83*, 397−410.
(40) Kaganer, V.; Kohler, R.; Schmidbauer, M.; Opitz, R.; Jenichen, B. X-ray Diffraction Peaks due to Misfit Dislocations in Heteroepitaxial Structures. *Phys. Rev. B: Condens. Matter Mater. Phys.* **1997**, *55*, 1793−1810.
(41) Pawlis, A.; Panfilova, M.; As, D. J.; Lischka, K.; Sanaka, K.; Ladd, T. D.; Yamamoto, Y. Lasing of Donor-Bound Excitons in ZnSe Microdisks. *Phys. Rev. B: Condens. Matter Mater. Phys.* **2008**, *77*, 153304.

DOI: 10.1021/acsaelm.8b00006
ACS Appl. Electron. Mater. 2019, 1, 44−50